Department of Physics and Astronomy
University of Heidelberg

Bachelor Thesis in Physics
submitted by

Robin Eberhard

born in Aalen, Germany

handed in on

April 1, 2016

Imaging of a degenerate Fermi gas of ultracold Lithium atoms

This Bachelor Thesis has been carried out by Robin Eberhard at the
Physics Institute in **Heidelberg**
under the supervision of
Prof. Dr. Matthias Weidemüller

Imaging of a degenerate Fermi gas of ultracold Lithium atoms

Robin Eberhard

Abstract   In this work, a double-species optical imaging system with high resolution was adapted and built into an ultracold mixture apparatus. The high quantum efficiency of the camera and its new readout mode, which allows for faster acquisition, are perfectly suited for scientific imaging of atomic density distributions. During this thesis, the electronic noise of the CCD detector was extensively characterized and a mechanical shutter was set up. The complete imaging setup was used to measure the density distribution of an ideal Fermi gas of ultracold Lithium atoms. Deviations from a thermal distribution and the transition in the degenerate regime with the minimal achieved $T/T_F = 0.34 \pm 0.26$ could be observed.

Zusammenfassung   In dieser Arbeit wird auf einem optischem Abbildungssystem mit einer hohen Auflösung angeschlossen, welches anschließend in ein Experiment mit ultrakalten zweiatomigen Gasen eingebaut wurde. Mit der hohen Quanteneffizienz und dem neuen Auslesemodus der Kamera ist diese perfekt für Wissenschaftliches Abbilden von atomaren Dichteverteilungen geeignet. Während dieser Arbeit wurde das elektronische Rauschen des CCD Detektors intensiv charakterisiert und ein mechanischer Shutter wurde aufgebaut. Das Abbildungssystem wurde benutzt, um Dichteverteilungen eines idealen Fermigases ultrakalter Lithium Atome zu messen. Abweichungen von einer thermischen Verteilung im Übergang zum degenerierten Regime wurden mit einem minimalen $T/T_F = 0.34$ beobachtet.

Contents

1. Introduction

Conducting experiments, measuring physical quantities and taking data are features that go hand in hand in scientific fields. Already in the early 1900s, imaging systems were chosen for data acquisition in astronomy. A complete optical system allowed for magnification of planets, our sun or nebulae. Already then, they were able to store their acquisitions on photo plates [1]. Nowadays so-called charge-coupled devices (CCD) or complementary metal-oxide-semiconductors (CMOS) are used as they can take the data digitally.

This also found application in the area of ultracold quantum physics — an experimental field that started around 1970s. In these experiments, atoms are prepared in traps at very low velocities, corresponding to the temperature regime around $1\,\mathrm{mK}$ and below. The atoms can then be detected by illuminating them with a laser beam, that is resonant with the atoms. The atoms will cast a shadow, which can be focused onto the chip, where the result is digitalized and can be analysed. Interesting physical quantities of atomic clouds are usually density distributions and atom numbers, since they contain a lot of information about various properties of the ultracold gas, for example, temperature, density or compressibility. In order to calculate atom numbers, a high resolution imaging system is not needed, since the optical density is extracted from the whole chip and not individual pixels. Therefore if the magnification of the system is known, one can directly conclude the atom number.

In order to directly probe interactions between atoms and the resulting distributions, an optical imaging system with a high resolution is commonly used. It consists of several lenses that are carefully set up in order to gain optimal resolution. A high number of pixels on the chip and high quantum efficiencies then allows to extract detailed information about the cloud. Especially for a small number of atoms it is additionally important to have small noise in the camera as well as a high sensitivity to photons.

Our experiment uses an ultracold mixture of ^{6}Li and ^{133}Cs atoms. This combination of atoms is particularly well suited for the study of the Efimov effect [2–4] and different polarons [5–7] (Fermi-polaron, Bose-polaron, Bubble-polaron). The interactions between Li and Cs atoms, that can be tuned by broad Feshbach resonances, will allow to explore various

few- and many-body effects. The study of all of these phenomena will require a well-tuned imaging system.

This thesis describes a double-species optical imaging system with high resolution that was adapted and built into the experimental apparatus. The setup features a new CCD camera with reduced noise and high quantum efficiency. A novel acquisition mode allows to drastically improve the acquisition timings. This thesis is structured as follows.

At first, the imaging setup is explained in Chapter 2.1. Chapter 2.2 then introduces the new camera used and highlights its qualities and improvements to the old system. In order to fully understand the noise properties of the chip, the basics of a CCD detector are explained, followed by measurements of different noise sources, for example the dark current, and the readout noise. Finally an overview about the quantum efficiency and how it affects the imaging quality is given.

A mechanical shutter was built into the imaging path. The shutter can be electronically controlled, in order to do that, a circuit was implemented in Section 2.3.1. The dynamics of the shutter were investigated to extract accurate timings of the opening and closing of the shutter.

Section 2.4 focuses on the new acquisition mode of the Andor camera, which requires to block parts of the chip. In order to do that, a slit was built and placed in front of the chip. The diffraction introduced by the slit was characterized and explained theoretically.

In Chapter 3 the imaging of an ideal Fermi gas is described. The density distribution of an ultracold cloud of harmonically trapped atoms is briefly explained in 3.2, the chapter concludes with measurements and analysis of temperature of an ideal Fermi gas of Li atoms.

2. Setup for high resolution imaging

In order to understand the nature of atoms in more detail, experiments are conducted where they are trapped and cooled. Under these circumstances, interactions between atoms can be tuned using Feshbach resonances. This allows to build up for example Bose-Einstein condensates (BEC) or Cooper pairs. The complete setup has been explained in more detail before [8]. The following sections will focus on the imaging in order to extract these attributes and the measures it takes to reduce noise sources on the camera.

2.1. Experimental requirements

In this double species experiment, fermionic ^{6}Li and bosonic ^{133}Cs are trapped and cooled inside a vacuum chamber. The atoms are emitted from an oven into a Zeeman slower, which transfers them into a magneto-optical trap (MOT). The MOT will further cool the atoms down to the Doppler limit (around $140\,\mu$K). To reach lower temperatures, the atoms will be trapped inside an optical dipole trap. Forced evaporative cooling will release the fastest atoms, until temperatures of a few tens of nano Kelvin are reached.

In order to image the atoms, an imaging beam is pointing along the z-axis according to Figure 2.1. An achromatic doublet lens focuses the imaging beam onto the CCD camera, which is located on top of the vacuum chamber.

In order to measure even at low atom numbers ($n = 1000$), the setup was refined allowing for high resolution [9]. The first lens, which collimates the image of the atoms has a low focal length of f=100 mm. The image is refocused into the camera by the second lens ($f = 750$ mm). Since the imaging uses two separate wavelengths to image both Lithium and Cesium, the chromatic shift introduced by the lenses will result in two different focal points for the images. This is compensated by a high focal length, which therefore allows the camera to be approximately in the focus of both images.
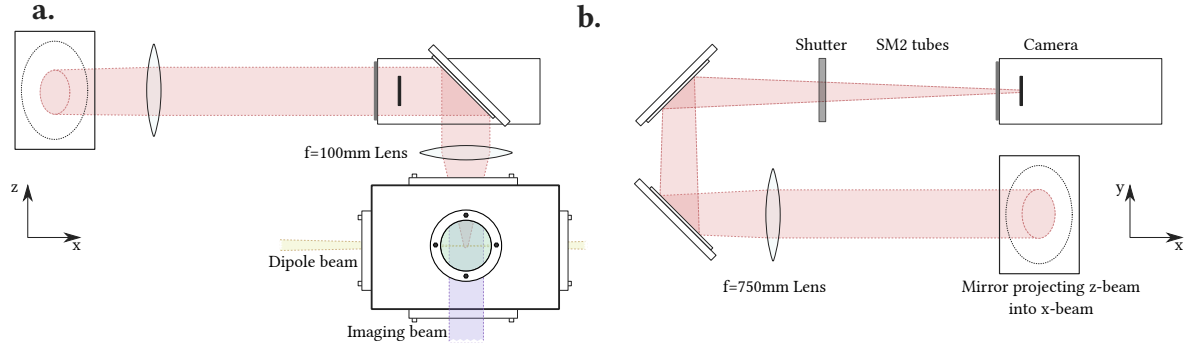
Figure 2.1.: **Imaging path.** The camera is mounted above the vacuum chamber as visible in **a.** (gravity would be in negative z direction). The image of the atoms is collimated with the first lens and passing the optics in **b.**, until it is refocused in the chip on the camera.

Having the first lens as close as possible to the atoms then allows for the highest resolution. With the high resolution of the camera it is then possible to take detailed images of atomic clouds.

2.2. Camera for double species imaging

The camera used in order to image atoms, the Andor iKon M [10], is a charge-coupled device (CCD). Using this camera, the dark noise, which a common effect on all CCD cameras, can be reduced, by cooling the chip, which are explained in the following sections. The camera also ships with a new acquisition mode, where it is now possible to take two consecutive images with only little delay.

2.2.1. Basics of CCD cameras

A camera operates by means of converting photons first into electrons then into voltage, which is finally read out as data [11, 12]. Each conversion process can add noise to the final image, which needs to be minimized in order to acquire accurate data.

The photons are collected on an array of semiconductor photo diodes, called the pixels, where ideally the spacing between the pixels is zero to gain maximum accuracy. The resolution is then dependent on the pixel size, which is usually between $10\,\mu\text{m}$ and $20\,\mu\text{m}$ per pixel for scientific cameras. Bigger pixels mean higher photon sensitivity but usually lower resolution.
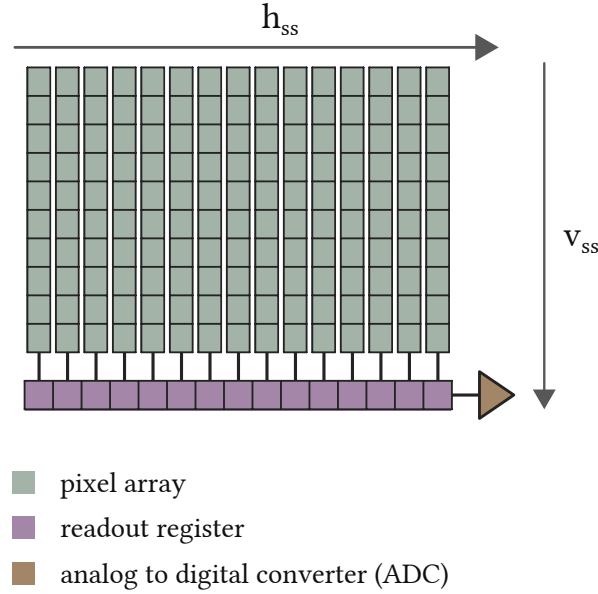
Figure 2.2.: **Schematic design of a CCD array and its readout.** The pixels are arranged in the pixel array. During readout they are shifted into the readout register and then to the side into the analog to digital converter (ADC).

To create a digital image, the charges from the pixels have to be shifted one-by-one into the analog to digital converter (ADC). This is done by vertically shifting them into the readout register and then horizontally into the ADC, where the charges are multiplied and converted to digital data. This is illustrated in Figure 2.2.

The shifting is done by storing the charges after collecting them, where each storage can be seen as an electronic potential well. In order to shift the charges and prevent overlapping, three spatially separated regions with potentials U_1, U_2 and U_3 are required. Figure 2.3 indicates the systematics behind the shifting.

Moving electrons to the next region is a three-step process. The charges are first only present in the region U_2, while the potentials U_1 and U_3 are kept high. They are then distributed across U_2 and U_3 by setting them both low. At last U_2 will be set high such that the charge is now fully in U_3. This is repeated until the charge has been finally shifted from pixel A to B, which in total takes seven steps.

2.2.2. Comparison with the previous setup

For the imaging of small atomic clouds, it is very important to have cameras with minimal noise and maximal readout speed. The new setup improves both. The dark noise, which is
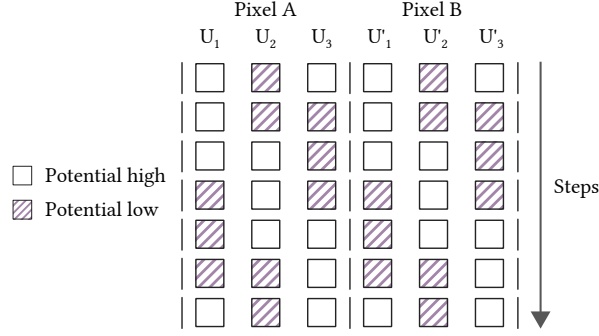
Figure 2.3.: **Shifting charges in a CCD detector.** To shift charges from Pixel A to Pixel B, the three potentials at the regions U_1, U_2 and U_3 in each pixel have to be set accordingly to allow the charge flow without overlapping each other. Each row represents a single step.

a temperature dependent effect, where counts accumulate over time, can be significantly reduced by cooling the chip down to less than $-70\,°C$. A new readout mode, called fast kinetics, makes it possible to acquire all images before reading out. This significantly improves the speed at which images can be taken.

The readout speed is highly important in our setup. Since absorption imaging is the technique of choice to measure atom attributes, three images need to be taken in each sequence, being the absorption, division and background image. The old setup used a Guppy-38B [13] camera, which has a frame rate of 30fps. This meant the acquisition was finished after $100\,ms$. The new Andor camera, on the other hand, can take images quickly without the need to read out in-between. At the fastest shift speed, the acquisition is finished after $1.632\,ms$, improving the speed by a factor of more than 60.

The quantum efficiency is explained in Chapter 2.2.5 and is also highly important, as it describes how many photons are detected on a camera and is directly connected to the sensitivity. A higher quantum efficiency therefore means better results. They compare as $QE_{Li} = 79\%, QE_{Cs} = 77.3\%$ for the Andor and $QE_{Li} = 35\%, QE_{Cs} = 10\%$ for the Guppy camera [9], for Lithium and Caesium respectively, as the QE is frequency dependent. Therefore the sensitivity of the new camera is significantly higher.

When comparing the resolution, the chip size also has to be considered. Since higher resolutions seem to be preferable at first, it also means that for the same pixel sizes, the photon sensitivities will decrease. The pixel sizes are $8.4\,\mu m * 9.8\,\mu m$ in the old setup and $13\,\mu m * 13\,\mu m$ in the new setup, while the resolutions are 768×492 and 1024×1024 respectively. This means that the new setup allows larger magnification.

The Guppy camera is a lot smaller than the Andor ($48.2\,\text{mm} \times 30\,\text{mm} \times 30\,\text{mm}$ vs $204.2\,\text{mm} \times 105\,\text{mm} \times 107\,\text{mm}$), therefore making an implementation on a full experimental table easier. To implement the complex imaging system surrounding the Andor camera, a lot of preparation was made in the thesis of Carmen Renner [9].

In spite of its large size, the new camera offers the ability to image both Lithium and Caesium species at once, while two Guppy cameras were needed beforehand, which also meant placing them on different imaging axes.

2.2.3. Dark current

A common noise source that is apparent in all CCD cameras, is the so-called dark current. It originates from the thermal excitation of electrons in individual pixels. Since they are made of semiconductors, once in a while, an electron can pass the potential between valence and conduction band simply due to their thermal energy. Thus, excess electrons accumulate, which contribute to the background signal and introduce additional noise [14].

The dark current has a strong temperature dependence [15]:

$$I_{dark}(T) \propto T^{\frac{3}{2}}\exp(-E_g/2k_BT), \tag{2.1}$$

where E_g is the band gap, that separates the valence from the conduction band in the semiconductor, T the temperature and k_B the Boltzmann constant. Therefore in order to reduce dark current noise, the temperature of the chip can be reduced, which decreases the thermal energy of the electrons.

This reduction of dark current with lower temperature has been measured and verified in Figure 2.4, using the built-in peltier element in the Andor camera to control the temperature of the CCD chip. For a long exposure time, dark current accumulates on all pixels. The counts are measured for several temperature settings and the counts C are converted to electrons per pixel per second (I_i) [15] for each pixel i as

$$I_i = \frac{C_i}{Gt_{exp,i}}, \tag{2.2}$$

with the Gain G of the camera, and the exposure time t_{exp}. The readout time of the pixels can be neglected, as it is significantly lower than the exposure time (see Chapter 2.4.1). The data should then follow the theory in Equation 2.1, although deviations are visible in the
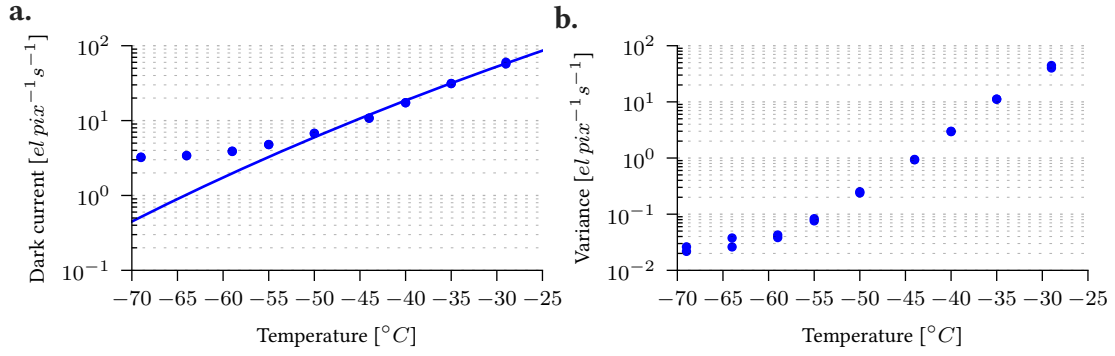
Figure 2.4.: **Dark noise accumulation on the chip.**   For a long exposure time of $100\,\mathrm{s}$, the dark current was measured for several temperatures. Gain in this measurement was minimal (0.215 [9]). Equation 2.1 was fitted, leaving the amplitude A and band gap E_g free, which resulted in $A = 1.1 * 10^8\,\mathrm{W\,m^{-1}\,K^{-1}}$ and $E_g = 0.96\,\mathrm{eV}$.

low temperature regime, which result from the internal fan not being able to divert the heat from the chip.

As it is important to minimize the noise source, the chip is cooled to the lowest possible temperature. This reduces the possibility of thermal electrons creating counts in the detector, so that even at small atom numbers, they are still distinguishable from the noise.

2.2.4. Readout noise

As described in Chapter 2.2.1, pixels are shifted in order to be read out by the ADC. Moving charges from pixel to pixel causes noise that accumulates over each iteration. Together with the noise which the ADC introduces, this is then called the readout noise. The shifting noise together with the dark noise is visible as a gradient (Figure 2.5) since each shift adds new charges due to excitations in the semiconductors. In order to characterize this, one can take the variance of the image, which should be zero for no noise.

In Figure 2.6, the readout speeds were probed for their noise. The measurement was carried out by taking images at short exposure time of $\sim\mu$s and low temperature of $T = -70\,^\circ$C, so that the main noise source would be from the readout and not the dark current. The variance of an image then indicates the noise accumulation on the chip and it has been shown, that slower readout speeds accumulate less noise, although it is only dependent on the horizontal, not on the vertical shift speed.
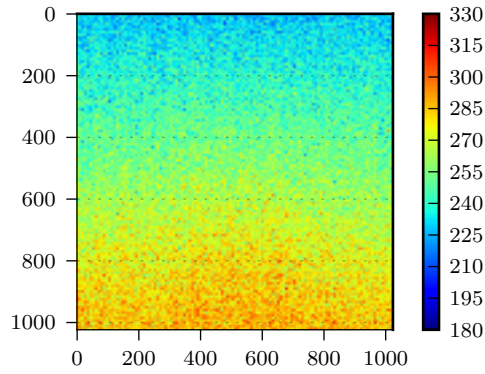
Figure 2.5.: **Gradient on the chip during readout.** Dark current accumulates on the chip over time. During readout, this is visible as a gradient, since the pixels that have not been read out are still affected by this noise. As the chip temperature is being lowered, the gradient will also decrease.

The actual readout of the chip can be done at slow speeds, so that the noise from horizontal shifting is low. As the vertical shifts do not add significant noise, it can safely be set to fast speeds, which is also favourable, as ^{6}Li and ^{133}Cs are imaged back to back as fast as possible, so that the cloud dynamics are still approximately the same.

Shifting charges means increasing and decreasing potential wells, so that they can move from one into the other. If this is done fast enough (non-adiabatic), electrons in the pixel are more likely to get excited from the valence to the conduction band from the semiconductor, therefore adding noise. As a consequence of these results, slower readout speeds are used in order to not add significantly more noise.
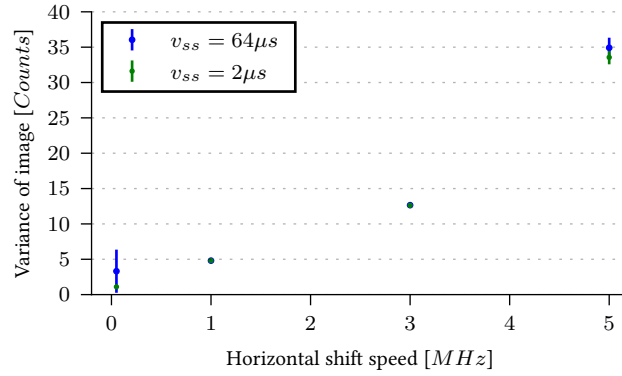
9

Figure 2.6.: **Readout noise.** The pixels are shifted row-wise into the readout register, depending on the vertical shift speed (v_{ss}) and then moved pixel-by-pixel with the horizontal shift speed into the analog to digital converter. Since noise reduction is important, minimal horizontal shift speeds will be used, while the vertical shift speed does not seem to affect the variance. To make the readout the dominant noise source, temperature was set to $-69\,°C$ and exposure to $10\,ms$. The results have been received from taking the mean and variance of multiple sets of exposures.

2.2.5. Quantum efficiency

When selecting cameras for scientific imaging, one of the attributes to look out for is quantum efficiency (QE). Not all incoming photons are converted into electrons, which adds an uncertainty and additional noise to measurements. This is characterized by quantum efficiency, which is defined as the fraction of photons that are converted into electrons. A QE of 100% would mean, that every incident photon is converted into an electron on the chip. This can be put into equations as

$$QE = \frac{N_{detected}}{N_{total}},$$ (2.3)

where $N_{detected}$ describes the number of detected photons and N_{total} the number of photons implying on the detector.

The measurement of the quantum efficiency has been previously carried out by Carmen Renner [9] in her diploma thesis. In order to do so, the number of detected photons can also be expressed in terms of the energy E_{beam} of all photons reaching the camera and the energy $E_\gamma = h\nu$ of a single photon [16]:

$$N_{total} = \frac{E_{beam}}{E_\gamma} = \frac{P t_{exp}}{E_\gamma},$$ (2.4)

where P is the beam power and t_{exp} the exposure time.

Now the quantum efficiency reads

$$QE = \frac{h\nu N_{detected}}{Pt_{exp}}.$$ (2.5)

In order to find the QE, one would now measure the accumulated counts for several exposure times, since the frequency ν and the power P are known. For the Andor camera used in our experiment, they have been measured as [9] 79.0 % for 671 nm and 77.3 % for 852 nm.

This camera was especially chosen for its quantum efficiency, since it is important in our case, to be able to detect most photons from Lithium and Caesium absorption.

2.3. Mechanical shutter

Due to the high quantum efficiency, the camera is very sensitive to stray light. Therefore it is necessary to cover the chip when it is not actively exposed. A mechanical shutter which can be electronically controlled is therefore built in front of the light path, which prevents the camera from damage between measurements. The electronics were set up and the shutter characterized in order to find perfect timings, so that light only enters the chip, when a measurement is running.

2.3.1. Electronic and mechanical setup

The high QE of the Andor camera translates into a high sensitivity of the CCD chip to stray light. Therefore, in order to not unnecessarily illuminate the chip, a mechanical shutter was built into the optical path, which can also be seen in Figure 2.1. By opening the shutter shortly before the imaging sequence and closing it immediately afterwards, the stray light that is implying the CCD detector can be minimized.

The shutter has five fans, as seen in Appendix B, which are mechanically guided, such that they together perform a circular motion outwards. The circular motion is best achieved for narrow fans, therefore needing more in order to close the shutter properly.

To shutter

TTL Control Input
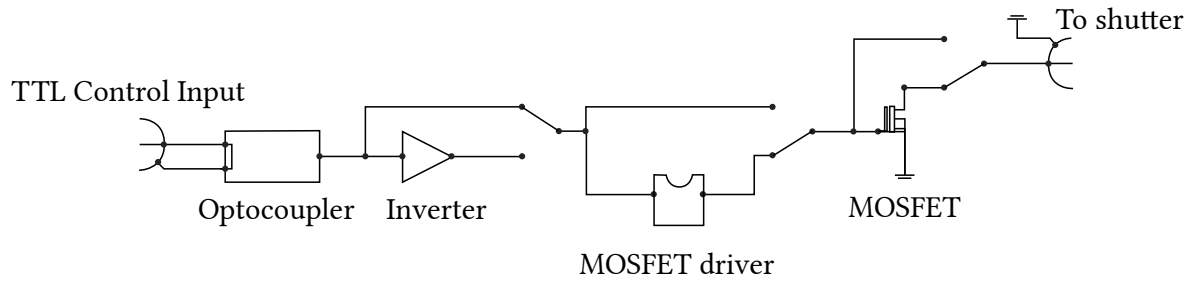
Optocoupler   Inverter

MOSFET driver

MOSFET

Figure 2.7.: **Electronic circuit to control the shutter.** The first element in the circuit is the optocoupler which is used to decouple parts from the circuit in order to not create loops, which would induce charges when the magnetic fields are on. The remaining parts can be skipped by setting the jumpers. The inverter will flip the sign on the voltage. The MOSFET driver is used in order to serve the correct voltage at the transistor's gate and to help during discharge, such that the MOSFET will not overheat. The transistor will finally serve a high current of 2.5 A, that is throughput to the shutter. The jumpers in this figure are set as they are used in the experiment. The complete circuit can be found in Appendix C.

The guides are connected to each other and can be pulled outwards with a mechanical switch, that can be manually pushed or pulled. To drive the shutter electronically, a magnetic coil and a magnet are used. When the coil receives a current, the magnet, which is connected to the switch, will pull the guides, moving them outwards, therefore opening the shutter.

Although the coil can pull the magnet in, it cannot be pushed away. This is compensated using a spring, which is connected to the switch. This also means, that the current driving the coil needs to be high enough to also work against the spring.

The optimal case would be now to have fast opening and closing times, since we want to prevent illumination between measurements. This can be achieved by testing several springs and to make the pull from the magnetic coils as fast as possible, which means increasing the current to drive it.

A custom circuit as shown in Figure 2.7 is used. In order to obtain a high current to increase the pull from the magnetic coil on the magnet, a transistor is implemented, which is controlled by a MOSFET driver. The complete circuit also contains a voltage regulator, so that the user does not need to know the input of the driver and can simply use a high voltage to open the shutter ($V \in [2, 8]$ V) and a low voltage ($V = 0$ V) to close it.
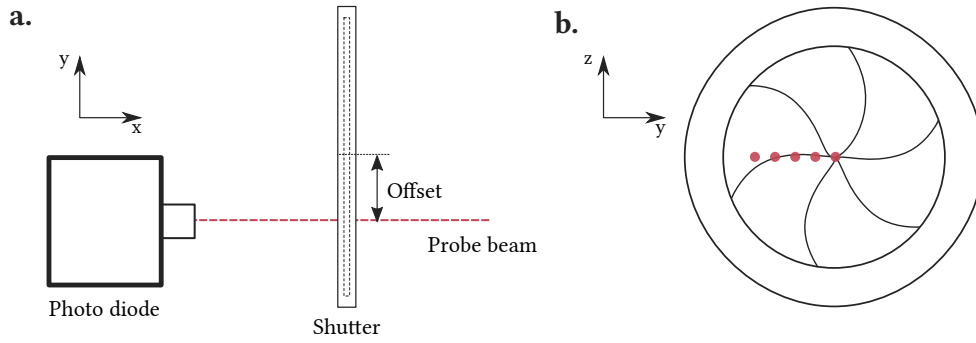
Figure 2.8.: **Probing the shutter for dynamics.** The shutter is proped at several positions using a laser. The offset in y direction was varied to find opening and closing times as a function of their offset.

2.3.2. Dynamical properties

The shutter operates by controlling a magnetic coil, which pulls a magnet. The magnet is reverted into its original position by a spring, closing the shutter. It was discussed before, in Subsection 2.3.1, that more fans give a better approximation to a circular motion. Optimally, we would expect the shutter to open perfectly circular with linear velocity. Therefore, to optimize on this, one would look at opening and closing speeds, which should be minimal.
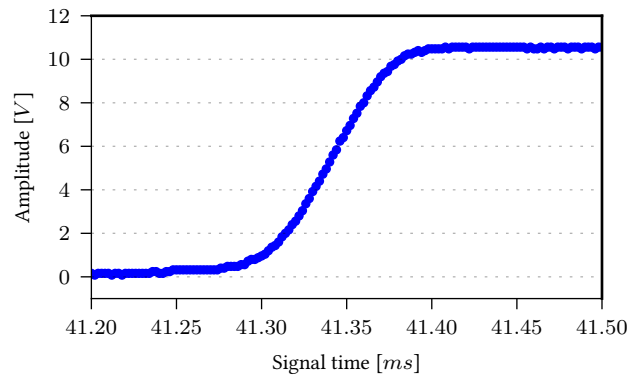

Figure 2.9.: **Shutter characterization.** The dynamics of the shutter were measured using a laser beam with a variable horizontal offset, which is fixed in this plot, and a photo diode measuring the laser intensity. In this figure, the offset is 9.3 mm from the centre. An error function was fitted yielding the time until the shutter opens. The opening time is defined here as the mean value of the error function, and was found to be 41.35 ms in this case.

To find the actual dynamics of the shutter, an experiment was set up. The shutter was probed at several positions, using a laser, to find the opening time. An example of one
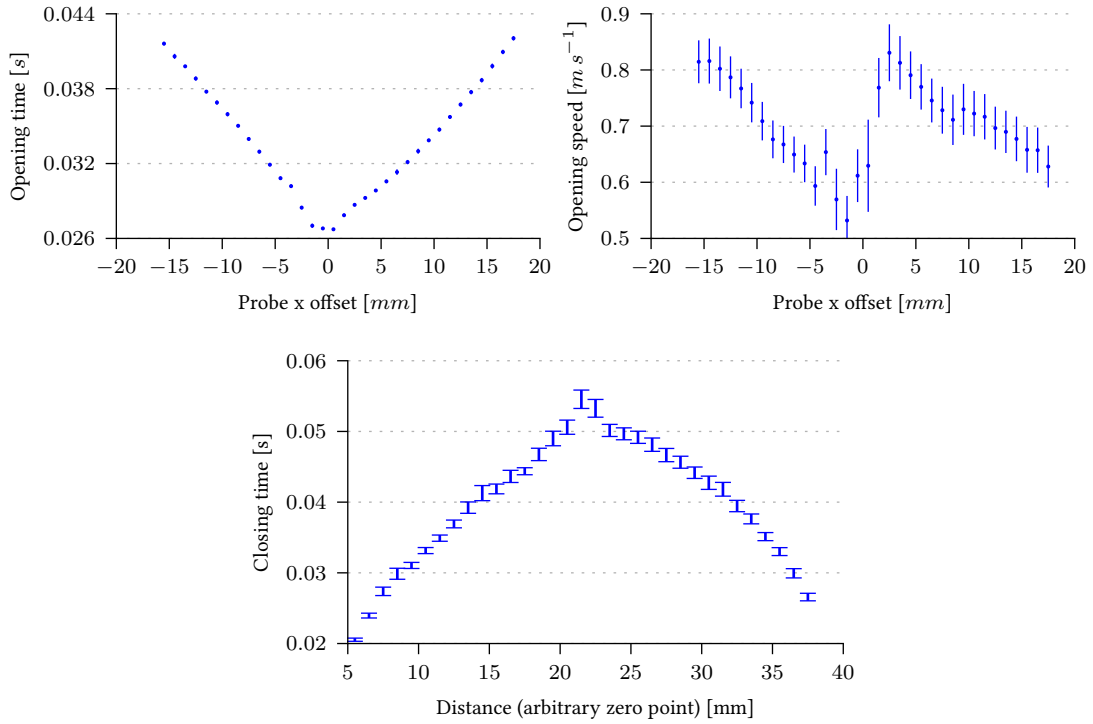
Figure 2.10.: **Sample dynamics.**   The figure shows opening and closing time as well as the opening velocity for a strong spring. The spring closed the shutter quickly while it prevented it from opening fast. The velocity was measured by using the gaussian beam diameter from the incident laser beam as the distance the shutter needed to transverse. For each offset, a set of 100 images were taken and the errors found as being the variance. It is noticeable, that the opening velocity on the right side is faster at first than on the left side. This is due to the structure of the shutter, as can be seen in Appendix B. The overall opening speed on the other hand is not affected by this and seems to be linear with the offset.

of many measurements is shown in Figure 2.9. The laser beam has a gaussian intensity distribution, which results in a error function on the photodiode as only partial intensity is received from the diode, when the shutter is still blocking parts of the beam.

The data points have been found by pointing a laser beam at a photodiode, which was blocked by the shutter. Since the laser has a finite radius, there is a transition in the signal from the minimum to the maximum, which is due to the approximately linear opening velocity of the shutter and the gaussian intensity distribution of the laser beam.

In order to find the opening and closing times of the shutter as seen in Figure 2.10a., the offset from the centre of the shutter was varied. For larger offsets, the time from the initial trigger until a signal in the photodiode was received is longer when the shutter is opening,
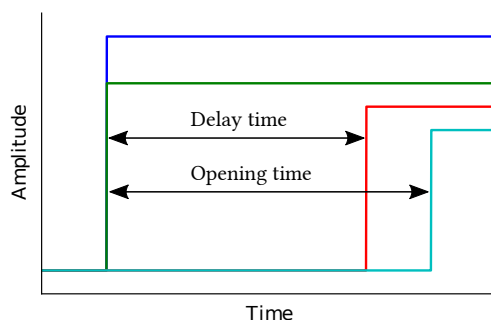
Figure 2.11.: **Shutter opening timings.**   In the figure, the four signals show the timings until the shutter is open. The blue signal is the trigger that is sent from the user to start the opening sequence. The electronics add some minor delay, which is about a few nanoseconds until they send out the green trigger. After a certain delay time, which is most likely due to the coil needing to accumulate charge first, the red signal indicates when the shutter starts to open at the centre. The opening sequence is finished, when the shutter is fully open, which is shown by the turquoise line.

while it is shorter when it is closing. In Figure 2.10b. the speed is not perfectly linear. The deviations close to the centre originate from the shape of the fans. As there are five fans, there is no mirror symmetry, so that opening to the left and right is different in the end.

The results will later be used to time the triggers in the measurement, so that the shutter can stay closed as long as possible. But in order to optimize it, there were two shutters at hand, and several springs to choose from, the combination of which were all tested until the optimal timings for opening $t_{open} = 12\,\text{ms}$ and for closing $t_{closing} = 14\,\text{ms}$ were found.

It has been found that the opening time actually consists of three timings. The initial trigger signal runs through the electronics, until it is sent to the shutter coil. The coil then has a delay, until it starts pulling the magnet. The opening time is then found by additionally adding the time until the fans are fully open. This is also shown in Figure 2.11.

2.4. Mask for the CCD sensor

One of the key features of the Andor iKon M is the fast kinetics readout mode. This allows for fast acquisition, which is important when imaging multiple species. Using this acquisition mode, we are able to take images $500\,\mu\text{s}$ apart from each other, so that it is possible to take consecutive images from the same cloud before it is too dilute. The acquisition mode is

explained in these sections as well as the diffractions introduced by a slit, which is needed to mask parts of the chip.

2.4.1. Fast kinetics mode

The fast kinetics mode allows the image acquisition timings to be only dependent on the vertical shift speed, reducing the acquisition time significantly. In this mode, only a portion of the CCD is illuminated, while the dark parts of the chip will be used as a storage. This means, that as soon as an image is taken, the illuminated pixels are shifted vertically behind a mask, such that no photons can reach them any more. When the chip is full or the user has finished their acquisition, the readout process is started.

As explained earlier in Chapter 2.2.1, the readout consists of first shifting a row into the readout register and then horizontally shifting them into the ADC. This is a very time consuming process, since the total readout time is described by

$$t_{ij} = iv_{ss} + (i - 1)j_{max}h_{ss} + jh_{ss}, \tag{2.6}$$

where v_{ss} and h_{ss} indicate the vertical and horizontal shift speed respectively. With this equation, the readout time until a pixel with the coordinates i and j is shifted into the readout register can be calculated. The readout of all pixels beforehand is also taken into account by j_{max} which is the width of the chip in pixels (1024 for the iKon M camera). As can be seen, in terms of the horizontal speed, the position of the last pixel in a row has a quadratic dependency. This is the dominant contribution to the readout time which is necessary to shift the pixels into the ADC. At this point, the speed should not matter too much any more, because the experiment is already finished and the pixels are not illuminated any more.

To set up the fast kinetics mode, there are several parameters that need to be set in advance.

- **Series length**. The number of images acquired before the readout phase is initiated.

- **Exposed rows**. The height of an image in the fast kinetic series.

- **Offset from bottom**. Number of rows from the bottom of the chip which are used as a temporary storage for the illuminated pixels.
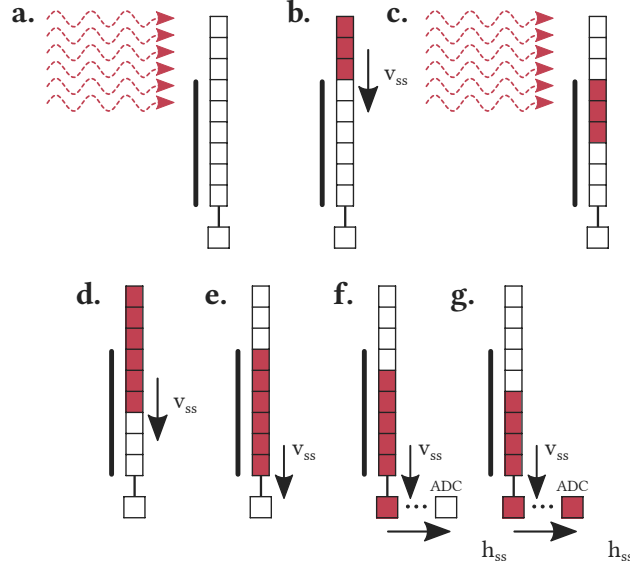
Figure 2.12.: **Schematics of imaging in the fast kinetics mode.** **a.** Laser photons excite electrons in pixels, creating the first absorption image. **b.** The illuminated pixels are shifted down behind a cover, while the laser is shut off. **c.** The second absorption image is taken without affecting the previous measurement. **d.** Both images are shifted down before starting the readout process, to not falsify the data with stray light. **e.** The readout process starts, the first row is shifted into the readout register. **f./g.** The first pixels are shifted into the ADC. It is repeated until the complete chip has been read out.

It can be easily seen that the parameters are limited by the height of the CCD in pixels:

$$\mathbf{Exposed\,rows} + \mathbf{Offset\,from\,bottom} \leq 1024\,\mathrm{px} \tag{2.7}$$

and

$$\mathbf{Series\,length} * \mathbf{Exposed\,rows} \leq \mathbf{Offset\,from\,bottom}. \tag{2.8}$$

Therefore, in our application, we chose an exposure of 204 px with an offset of 820 px, which gives a series length of 4. The pixels that are used as temporary storage of accumulated charge until the readout process begins need to be shielded from light. This is achieved with a slit in front of the camera that blocks part of the light beam implying on the CCD detector.

Since we will be imaging two atomic species, an absorption image for each species will be followed by two division images, as well as background images to subtract the noise, which is further explained in Section 3.1. The fast kinetic mode now allows us to do this quickly, which is important when imaging multiple species together.
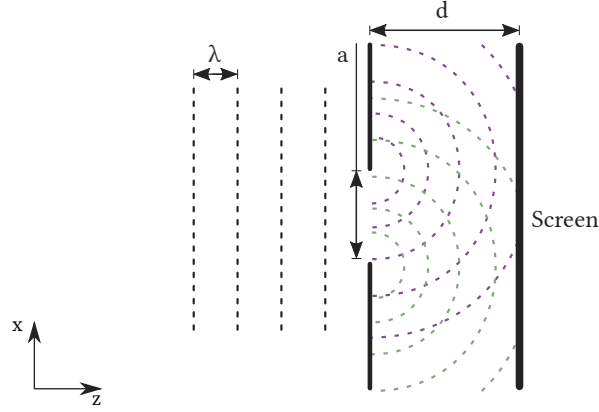
Figure 2.13.: **Diffraction on a single slit.** A planar wave with the wavelength λ approaches a slit with a width a, where the maxima of the wave are drawn as dashed lines. After the slit, Huygens principle is visualized by spherical waves, (purple and green), interfering with each other. The new wavefront is created where the waves intersect each other and is as such visible on the screen to the right.

2.4.2. Frequency response of a slit

The slit is an optical element in the path, which will introduce diffraction — an effect due to the wave nature of light. Figure 2.13 sketches the systematics behind a plane wave approaching a slit.

The incoming planar wave can be described by the electric field:

$$E(z) = E_0 e^{-ikz}, \tag{2.9}$$

where the wave is propagating in the z-direction with the wave number k and an amplitude E_0.

It is known from Huygens principle, that each point of a planar wave can be seen as the origin of a spherical wave. The spherical waves will interfere with each other and because of the superposition principle a new wavefront will be built up. The mathematical formalism of Huygens principle is simply the sum of all spherical waves, which for infinitely small distances is given as [17]:

$$E(x, z) = E_0 C \int_{Slit} \frac{1}{r^2} \exp(-ikr) \mathrm{d}x'. \tag{2.10}$$

Here, $r = \sqrt{(x - x')^2 + z^2}$ is the radius of a two dimensional wave, C is a normalization constant. Taylor expansion of the radius for large z allows us, to substitute r^2 with z^2 and r

with $\frac{(x-x')^2}{2z} + z$, while also the approximation $(x - x') \ll z$ needs to be fulfilled. Therefore we get:

$$E(x, z) = E_0 e^{-ikz} \sqrt{\frac{ik}{2\pi z}} \int_{Slit} \exp\left(-\frac{ik}{2z}(x - x')^2\right) dx'. \tag{2.11}$$

The normalization was derived from the gaussian normal distribution $\exp(-\frac{ik}{2z}(x - x')^2)$. The integral will run over the slit size, with the origin in its middle and width a. We want to also write the exponential as a function of $-\frac{i\pi t^2}{2}$, due to the definition of Fresnel integrals. The substitution follows:

$$\frac{k}{2z}(x - x')^2 = \frac{\pi t^2}{2}, \tag{2.12}$$

$$\Rightarrow t(x') = \sqrt{\frac{k}{z\pi}}(x - x'), \tag{2.13}$$

$$\Rightarrow dx' = -dt\sqrt{\frac{z\pi}{k}}, \tag{2.14}$$

such that the field becomes

$$E(x, z) = -E_0 e^{-ikz} \sqrt{\frac{i}{2}} \int_{t(-a/2)}^{t(a/2)} \exp\left(-\frac{i\pi t^2}{2}\right) dt. \tag{2.15}$$

The Fresnel integrals are defined by

$$C(x) = \int_0^x \cos\left(\frac{\pi t^2}{2}\right) dt, \tag{2.16}$$

$$S(x) = \int_0^x \sin\left(\frac{\pi t^2}{2}\right) dt, \tag{2.17}$$

so that in combination with Eulers equations and splitting up the integrals the equation for the electric field is:

$$E(x, z) = E_0 \sqrt{\frac{i}{2}} e^{-ikz} \left[C(t(-a/2)) - C(t(a/2)) - iS(t(-a/2)) + iS(t(a/2))\right]. \tag{2.18}$$

In a real experiment, the light on a CCD chip is detected as intensity, which is given by

$$I(x, z) = \frac{2|E(x, z)|^2}{\epsilon_0 c}, \tag{2.19}$$

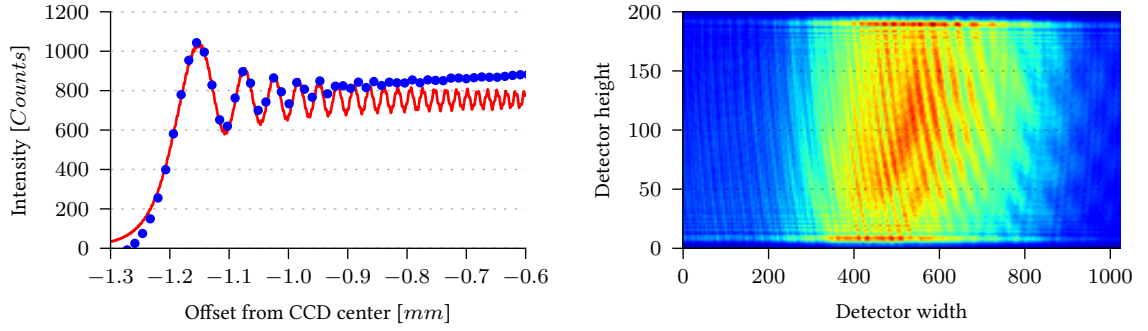with the dielectric constant ϵ_0 and the speed of light c.

Figure 2.14.: **Measuring diffraction on a slit.** In order to characterize the diffraction by the slit, the CCD detector was placed as close as possible. The parameters were measured using a ruler and yielded distance $d = (10.9 \pm 0.5)\,\text{mm}$, opening $a = (2.5 \pm 0.5)\,\text{mm}$. The wavelength was $\lambda = 852\,\text{nm}$ found from the laser specifications. The blue curve is the experimental data, while the red curve was fitted, leaving the distance and opening as free fitting parameters. They were found to be $d' = (11.0 \pm 0.3)\,\text{mm}$ and $a' = (2.470 \pm 0.013)\,\text{mm}$, which is in close agreement with the measured values. The residual deviation in the amplitude are caused by Gaussian intensity distribution of the laser beam used for illumination.

To verify the theory, we set up a simple experiment with a collimated laser beam pointing at the CCD of the Andor camera, with a slit in between. The predicted interference fringes were observed in our experiment. Figure 2.14 shows the diffraction pattern that was recorded with the Andor camera and a slit. A large, collimated beam was used to illuminate a slit in front of the CCD detector, which casted the diffraction pattern on the chip. Using the theoretical description, we were able to extract the slit width $a = (2.470 \pm 0.013)\,\text{mm}$ and the distance to the chip $d = (11.0 \pm 0.3)\,\text{mm}$.

The experimental diffraction pattern matches the theory very well, since the deviations are in the expected regimes. The function washes out as it approaches the centre of the chip. This is due to the nature of the pixels, which only have a finite size and the fact, that the frequencies of the oscillations are lower on the outer ends. All oscillations that fit into one pixel are averaged, therefore diffraction is not visible.

This result helps to minimize the diffraction on the chip and serves as a starting point in order to optimize this effect.
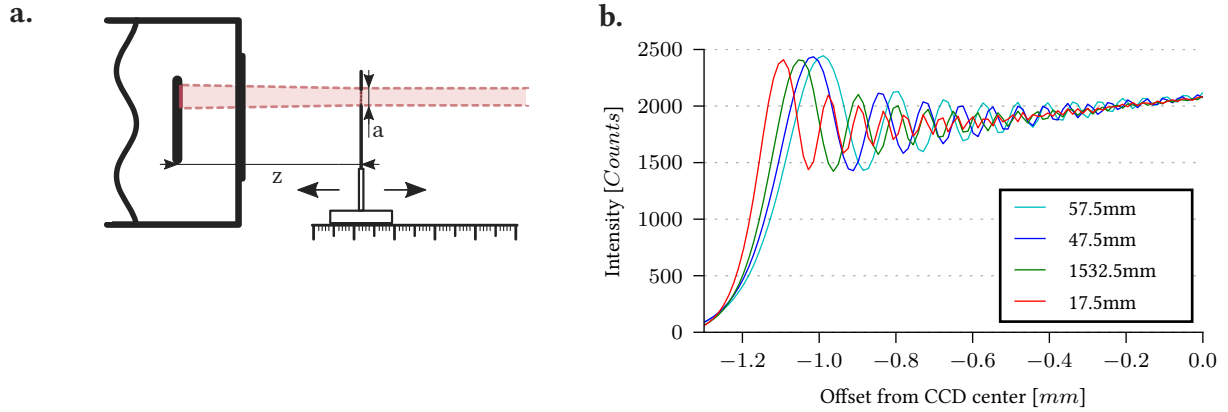
Figure 2.15.: **Distance dependent diffraction.** **a.** A slit was placed on a movable plat-form and diffraction was measured for various offsets z, while the slit opening a was kept constant. **b.** The diffraction frequency rises as the distance gets closer to the CCD.

2.4.3. Optimization of the masking setup

An important issue in the optimal placement of the slit is the distance from the CCD de-tector at which it is going to be placed. The frequency of the diffraction patter depends on the distance d; it is larger for smaller d, and smaller for larger d. In the limit $\frac{a^2}{d\lambda} \ll 1$ the diffraction pattern of a point source is recovered (Fraunhofer diffraction in the far field).

This dependence on the distance was also tested experimentally and the results are shown in Figure 2.15. The signal in one pixel is the average over all oscillations, that fit into the width of the pixel. Therefore the optimal slit position is close to the chip, since then the frequencies are maximal.

3. Thermometry of an ultracold Fermi gas

The purpose of the camera is to measure distributions of atoms from which important physical quantities can be extracted. Dense atomic clouds consisting of Lithium and Caesium, the improvement of the resolution in the whole imaging setup now allows to explore new features that could not be detected before. As an example, the thermometry of an ultracold ideal Fermi Gases will be discussed in this chapter. At very low temperatures, the gas undergoes a phase transition from thermal into a degenerate state. This is reflected in the density distribution, which differs from a gaussian profile that one expects for a thermal gas.

These changes are small, nevertheless, they can be detected with the new setup. Therefore, this chapter starts with a brief introduction to absorption imaging in Section 3.1, which is used to image the atoms. Afterwards, the density distribution of ultracold, ideal Fermi gases in harmonic confinement are explained in Section 3.2. Finally, in Section 3.3, the performed experiment with an ultracold gas of Li atoms and their analysis are presented.

3.1. Absorption imaging

In order to find microscopic properties of atoms, or assembles of atoms, it is necessary to look at the atoms themselves. This is commonly accomplished using either fluorescence or absorption imaging [18]. In both cases, a laser beam is pointed at an atomic cloud, that is cooled and confined in a trap. In fluorescence imaging, the scattered light is collected, typically in a direction that is different than the illuminating beam. The intensity from the light reaching the detector is not very high, since it is radiated in all directions. Therefore, long exposure times are required during which atoms can move and the information about the initial density and energy distribution is lost. Nevertheless, this approach is useful for single- and few-atom detection.

In contrast, in absorption imaging [18], the transmitted intensity of an imaging beam is recorded. Without atoms, one would detect the beam profile of the laser beam. With atoms, a shadow is visible due to the atoms "blocking" the light. This is accomplished, by correctly tuning the laser to a resonance frequency of the atoms, which enables them to absorb the light, exciting them to a higher state. Through spontaneous emission, the atoms will decay, making it possible to excite them once again. This method works well, when the "signal" from the absorbed light is significantly larger compared to the noise sources, and the atomic transition used for imaging is "closed", i.e. the excited atoms decay only into the imaging state.

In order to extract physical properties of the atoms after they have been illuminated, a quantity called optical density OD is found in the absorption profile, which has an exponential dependency to the intensity reaching the CCD. From the optical density, one can conclude for example atomic distribution and atom numbers. This is put into equations as follows [18]:

$$I_{CCD} = I_0 e^{-OD} + I_{back},\tag{3.1}$$

which is decreasing from the initial intensity I_0 as the light is scattered by atoms. The intensity I_{back} describes the background signal, that is found when the CCD is not being illuminated by a laser such as readout noise, dark noise or stray photon light. All the features of atoms are contained in the optical density, therefore in order to extract that, a background frame is subtracted from the absorption image and the laser profile divided, leaving

$$\frac{I_{CCD} - I_{back}}{I_0} = e^{-OD}.\tag{3.2}$$

The laser intensity I_0 is measured in a separate frame, containing the laser intensiy $I_0' = I_0 + I_{back}$ and also the background I_{back}. Finally, for each pixel of the CCD detector, the equation yields

$$\frac{I_{CCD} - I_{back}}{I_0' - I_{back}} = e^{-OD}.\tag{3.3}$$

From the resulting distribution of optical density, one can now extract, for example, atom density distributions, atom numbers or excitation rates.

3.2. Density distribution of an ideal Fermi gas

An ideal Fermi gas consists of atoms, that all occupy the same internal state and are thus indistinguishable. This way, each energy level in the trapping potential is occupied by one

or zero atoms up to the chemical potential μ, so that the fermions do not interact with each other. This leads to a density distribution of the atoms, which, depending on the temperature T and the chemical potential, can range between a common thermal distribution or a Fermi distribution for a degenerate cloud of atoms.

The fermionic cloud is characterized by the degeneracy parameter T/T_F, there T_F is the Fermi temperature, which corresponds to the chemical potential for $T = 0$. For values $T/T_F \gg 1$ the gas is then called thermal and will follow Maxwell-Boltzmann statistics. The cloud is called degenerate for $T/T_F \ll 1$ and the density profile will be a Fermi distribution. This is described by a shape parameter $q = \frac{\mu}{k_B T}$ with the Boltzmann constant k_B, which is large and negative in the thermal and large and positive in the degenerate regime. In this way, both the regimes are connected by tuning q.

In order to find out if the cloud is thermal or degenerate, one can fit a distribution, that interpolates between both regimes. The following derivations can be found in [20].

In the Gaussian distribution, the width σ_i is defined by

$$\sigma_i = \sqrt{\frac{2k_B T}{mw_i^2}}, \tag{3.4}$$

where m is the mass of Lithium and w_i is the trapping frequency in the $i = \{x, y, z\}$ direction of the cloud. Due to the alignment of the dipole trap, the cloud will not have a spherical shape and will therefore have different radii [21].

In the degenerate regime however, the atom density is best described by a Thomas-Fermi distribution with the Fermi radius

$$R_{Fi} = \sqrt{\frac{2E_F}{mw_i^2}}, \tag{3.5}$$

where $E_F = \hbar\bar{w}(6N)^{1/3}$ is the Fermi energy (N being the number of atoms and $\bar{w} = (w_x w_y w_z)^{1/3}$ is the geometrically averaged trapping frequency).

Experimentally, it is very hard to prepare a purely degenerate Fermi gas, such that a typical density distribution will contain contributions also from the thermal fraction of atoms. Therefore a unified radius,

$$R_i^2 = \frac{2k_B T}{mw_i^2} f(e^q), \tag{3.6}$$

can be used, with the previously declared shape parameter q. It smoothly interpolates between the two regimes and is used in fitting the atom density distributions. The interpo-

lation function $f(x)$ is

$$f(x) = \frac{Li_1(-x)}{Li_0(-x)} = \frac{1+x}{x} ln(1+x), \tag{3.7}$$

where Li_n is the n-th order polylogarithm and can be defined as

$$Li_s(z) = \sum_{k=1}^{\infty} \frac{z^k}{k^s}. \tag{3.8}$$

In our case, we integrate over all but one axes, and therefore the fitting function for the doubly integrated atom density distribution yields

$$n_{1D}(x) = n_{1D,0} \frac{Li_{5/2}\left(\pm\exp\left[q - \frac{x^2}{R_i^2} f(e^q)\right]\right)}{Li_{5/2}(\pm e^q)}. \tag{3.9}$$

During fitting, the shape parameter $q = \frac{\mu}{k_B T}$ is extracted, which describes the ratio between chemical potential and thermal energy of the gas.

In order to calculate the degeneracy parameter T/T_F, the value of q is inserted into the equation:

$$\frac{T}{T_F} = \left[-6Li_3(-e^q)\right]^{-1/3}. \tag{3.10}$$

As the imaging system only has a finite resolution, the cloud can be released and imaged after a short time. At the time of the acqusition, the gas will have expanded, although the distribution is approximately the same. During expansion of the cloud, the temperature, which is dependent on the radius, will not change. Therefore, the radius is contracted in order to receive the radius of the inital distribution by

$$R_{0,i} = \frac{R_i}{\sqrt{1+w_i^2}}, \tag{3.11}$$

which can then be used to calculate the temperature of the cloud using

$$T = \frac{1}{2} \frac{m w_i^2}{k_B} \frac{R_i^2}{1+w_i^2 t^2} \frac{1}{f(e^q)}. \tag{3.12}$$

3.3. Preparation and imaging of an ultracold Fermi gas

In order to conduct an experiment involving an ideal Fermi gas, fermionic Lithium atoms were cooled and captured with standard laser cooling techniques [2, 13]. Starting with a magneto-optical trap, D1 cooling was applied, from where the atoms were loaded into an optical dipole trap. Afterwards, the fermions were cooled even further using evaporative cooling, by reducing the power of the dipole beams. Naturally, the atoms are distributed in the lowest two spin states, which helps with the evaporative cooling process, as the atoms need to rethermalize. This is only possible, if the atoms can collide with each other. In order to create an ideal Fermi gas, one spin component is removed by resonantly exciting them with a laser pulse, which will not affect the other component, leaving them in the trap. Atoms were prepared for several trap depths in order to observe the gradual change between thermal and Fermi density distribution.

The cloud was imaged using the new imaging system, yielding the results in Figure 3.1. The atoms can be seen as a cloud which is larger in x than in y direction, which is due to the geometry of the optical dipole trap.

In order to extract the physical quantities from the density distribution, Equation 3.9 was fitted to the optical density of the absorption image, leaving q, $n_{1D,0}$ and R_i as free parameters. The fitted values are tabulated in Table 3.1. The doubly integrated distribution along the x axis displays large noise, which is most likely due to the suboptimal alignment of the optical setup, at the moment of the writing of this thesis. Therefore, the fit in the x direction was included in Figure 3.1, but the fit parameters are not presented as they are most likely not accurate. On the y axis, a linear gradient is visible. This is an effect of the readout of the chip and was fitted as well, but does not affect the physics as it does not interfere with the original fitting function.

From the fit parameters, the temperature and degeneracy parameter were calculated, which are found also in Table 3.1. Additionally, a temperature T_{tof} was obtained by taking a time of flight measurement from a different camera, which relates the expansion of the cloud to the velocity and therefore to the temperature of the gas.

From the results, we find that there is a match between the temperatures, although the temperature extracted from the Fermi distribution is probably better, since it includes the degenerate fraction as well. This is especially true for the two lower trap frequencies, where the shape parameter q indicates that the cloud is more degenerate than thermal.

As a cross-check, we fitted a gaussian distribution and extracted the "goodness" of the fit χ^2. As the cloud is not yet deeply degenerate for our values of T/T_F, the gaussian and Fermi
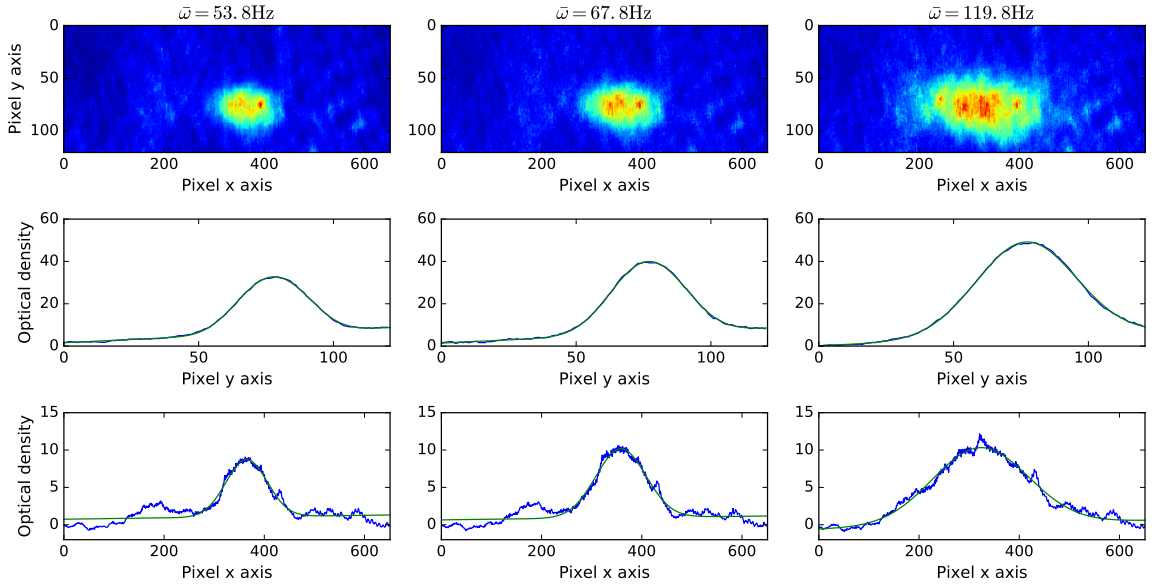
Figure 3.1.: **Fitting the Fermi distribution to an ultracold gas of Li atoms.** The atoms were imaged at three different trap depths which correspond to different $\bar{\omega}$. The upper row are false-color images of atom density distributions. As of the writing of this thesis, the imaging system was not yet well aligned, therefore large noise is observed in the distributions along the x axis (bottom row). The blue curve is the doubly-integrated signal from the image in the first row, and the green curve is the fit that was applied. The results of the fits in y direction (middle row) are given in Table 3.1.

distributions should fit approximately the same, while we would expect larger deviations for $T/T_F \ll 1$. We compared χ^2_{Fermi} of the Fermi distribution to χ^2_{Gauss} of the Gauss distribution with the values $\chi^2_{Fermi} = 1.71$ and $\chi^2_{Gauss} = 1.85$ for the trapping frequency $\bar{w} = 53.8\,\mathrm{Hz}$. This tells us that, although the gaussian distribution still fits the data very well, Fermi-fit is already sensitive to changes in the shape of the cloud. This is substantiated furthermore by the fact, that the extracted temperature T and T_{tof} from the Fermi fit and the time-of-flight measurement, respectively, are in good agreement.

$P[mW]$	43.4	77.0	255.0
$\bar{\omega}[\text{Hz}]$	53.8	67.8	119.8
n_{1D}	25.6 ± 0.1	34.07 ± 0.13	44.98 ± 0.24
q	1.87 ± 0.35	1.08 ± 0.34	-2.0 ± 1.85
$R_y[\text{µm}]$	41.4 ± 1.3	41.3 ± 1.3	46.4 ± 1.8
T/T_F	0.34 ± 0.26	0.42 ± 0.23	1.01 ± 0.56
$T[\text{nK}]$	59.2 ± 6.0	117 ± 15	536 ± 95
$T_{tof}[\text{nK}]$	56	97	480

Table 3.1.: **Fit parameters for various trap depths.**   The density distributions were fitted using Equation 3.9 for various trapping frequencies $\bar{w}$, which were tuned by setting the power P of the dipole laser beams. The parameter n_{1D} describes the amplitude of the peak. q is a shape parameter, which is negative if the cloud is thermal and positive if the cloud is degenerate. R_y is then the clouds radius. An additional temperature was calculated from a time of flight measurement, from a calibrated camera and was included in the table for comparison.

4. Conclusion and outlook

In this thesis, a new imaging setup was implemented, which increases significantly the resolution of the present absorption imaging. The Andor iKon M camera was introduced and the schematics behind a CCD chip were explained, leading to an understanding of various noise sources. As the pixels in a camera are made of semiconductors, we found that a common noise source is the so-called dark noise, where thermal electrons are excited to the valence band, creating counts. This can be prevented by cooling the chip down. We found that at $-70\,°C$, the dark current was already reduced to less than 4 electrons per pixel and second. Another common noise source was found to be the readout noise, which accumulates by shifting pixels into the readout register and the ADC. As the readout is dependent on the vertical and horizontal shift speed, we found that the noise does not depend on the vertical shift speed. Therefore we concluded, that during measurements the horizontal shift speed has to be low, while the vertical shift speed can be high in order to allow for fast acquisition of multiple images as they are read out using the fast kinetics mode.

Using this acquisition mode, it is possible to acquire images without reading them out in between. This is done by illuminating only a part of the chip. When the exposure is finished, the illuminated part is shifted down behind a cover, so that the top part is ready for the next image. This is an important feature of the camera, as the group is using a mixture of ^{6}Li and ^{133}Cs, which need to be imaged consecutively as fast as possible.

In the end, the new imaging system was tested on an ideal Fermi gas. Fermionic Lithium atoms were prepared in an optical dipole trap with only one spin component. We observed that the distribution of the atoms follows a Fermi-distribution for $T/T_F < 1$. For several trap depths, the degeneracy parameters were found to be $T/T_F = 0.34 \pm 0.26, 0.42 \pm 0.23, 1.01 \pm 0.56$ corresponding to the trapping frequencies $\bar{w} = 53.8, 67.8, 119.8\,Hz$ respectively.

From the details of the distributions due to the high resolution of the imaging setup, we were able to distinguish the density profile of the fermionic cloud from a gaussian shape, which already shows the potential of the imaging system. Building on that, one could now

also create fermionic superfluids, using a spin mixture. This state has a unique structure, where there is an unpolarized core surrounded by the majority spin component [22, 23]. The latter is then as well described by the same formulas as the polarized Fermi gas, which was also discussed in this thesis. This would be an exciting experiment as it will further put the resolution of the imaging system to a test.

A. Acquisition sequence

During absorption imaging, the Andor camera will take eight images, which consist of two absorption, two division and four background images (or if the user specifies to only image one species, then there is one absorption and division image and six background images).
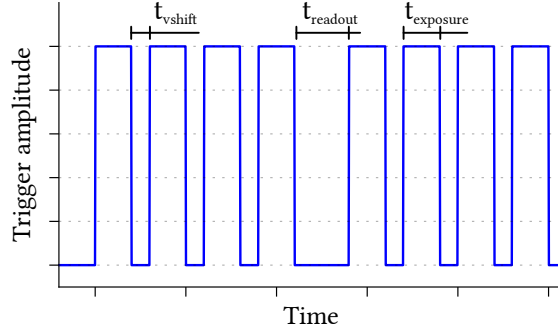
Figure A.1.: **Trigger signals.** The triggers are sent as a rectangular signal. The camera will interpret the rising edge of the signal as the starting point of the exposure. Here, t_{vshift} is the time it takes to shift the illuminated pixels downwards, $t_{readout}$ is the time it takes the chip to read out the data and $t_{exposure}$ the exposure time.

As the camera is only interested in the rising edge of the signal, the trigger length is not really important. But the chip will be exposed for the duration of the exposure time, after which the laser should be turned off. The, in our case, 204 pixels are then shifted downwards, taking t_{vshift}, which can be calculated by multiplying the vertical shift speed with the pixel height. For the fastest shift speed, this would result in

$$t_{vshift} = 2\,\mu\text{s}\,\text{px}^{-1} * 204\,\text{px} = 408\,\mu\text{s}, \tag{A.1}$$

for the slowest speed we find

$$t_{vshift} = 64\,\mu\text{s}\,\text{px}^{-1} * 204\,\text{px} = 13.1\,\text{ms} \tag{A.2}$$

Therefore the four subsequent signals can be taken after

$$t_{trig} = t_{vshift} + t_{exposure}. \tag{A.3}$$

Four images are acquired until the readout process is started. This takes significantly longer, but as explained in Chapter 2.4.1 can be calculated via:

$$t_{ij} = i * vspeed + (i - 1) * j_{max} * hspeed + j * hspeed. \tag{A.4}$$

For the whole chip, this gives us $i = 4 * 204 = 816$, $j = 1024$, $j_{max} = 1024$, therefore

$$t_{readout} = 816 * vspeed + 816 * 1024 * hspeed. \tag{A.5}$$

The minimal timings for an individual trigger signal t_i for the frame i can finally be calculated via

$$t_n = \begin{cases} (n - 1)t_{rig} & n < 5 \\ (n - 1)t_{trig} + t_{readout} & n \geq 5. \end{cases}$$
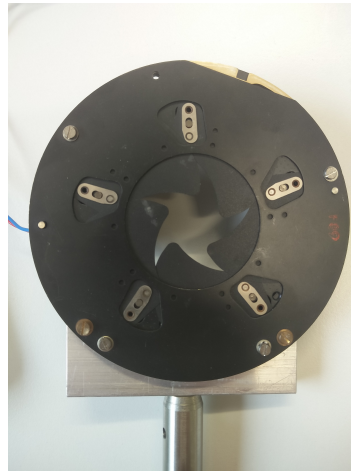
B. Design of the shutter

Figure B.1.: **Front view of the shutter.** Five fans are visible on the shutter as well as the mechanical guides, used to pull the fans outwards.

Figure B.2.: **Back view of the shutter.** The magnet is connected to the lever, which pulls the fans outwards.

C. Shutter circuit

The circuit given on the next page is the complete circuit as opposed to Figure 2.7. The key difference here, is that the actual board contains two input/output ports and there are also converters (visible in the top-left corner), that keep the voltage at 24 V, which is necessary in order to use the MOSFET driver.

The breadboard on the bottom are built into the circuit, so that custom additions can be made, although this is not used in our case. This circuit is commonly used in various labs in the institute, if high currents are required and was designed by Gerhard Zuern. The jumpers were set as they are used in our experiment. Input one was left out as it is not used at this moment. Additionally, a MOSFET was soldered onto the board as it is not implemented by default.

D. Setup of the custom slit

The cover, which can be seen in Figure D.1 has a width of 12.5 mm, which adds additional space before the chip. The cover is mainly for a manual cap to cover the chip, when the camera is not used, and an internal shutter. Since we knew, that the internal shutter was not needed, we were able to remove the cover bringing the slit closer to the chip.

The holes for M4 screws were already there, so a custom plate was built on which the slit could be mounted on. In the technical drawing in Figure C, the centre-most holes are reserved for the slit, which can be moved up and down to select the appropriate height needed for the imaging. The plate also gives the opportunity to move the whole set with the long holes in the outer-most edges.

It is also important to note, that the camera is very sensitive to stray light due to the high quantum efficiency. Therefore it is necessary to cover the laser path. The plate offers another set of screw holes, which will hold a SM2-mount, therefore eliminating any gap that could allow photons to reach the camera externally.

The long path of SM2 tubes then only allows the smallest amount of stray light to enter the camera, which will have significantly lower intensity than the actual absorption image.
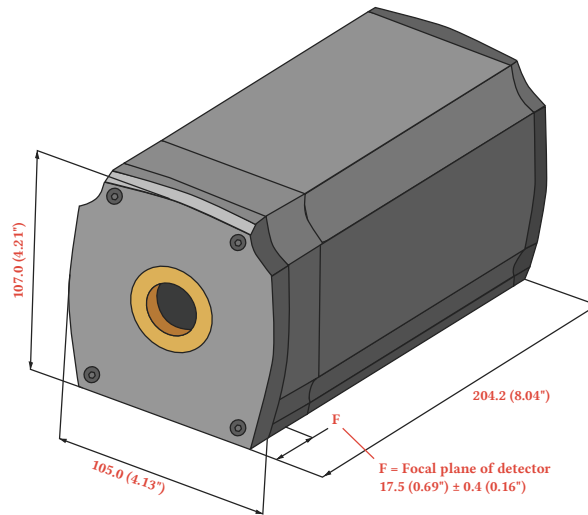
Figure D.1.: **Drawing of the camera.** As can be seen in this drawing, the CCD chip is first hidden behind a cover, that also includes an internal shutter and then offset by an additional 5 mm.

List of Figures

Bibliography

[1] University of Heidelberg. `http://dc.zah.uni-heidelberg.de/lswscans/res/positions/q/form`. Accessed: 28.03.2016.

[2] R. Pires, J. Ulmanis, S. Häfner, M. Repp, A. Arias, E. D. Kuhnle, and M. Weidemüller. Observation of Efimov resonances in a mixture with extreme mass imbalance. *Phys. Rev. Lett.*, 112:250404, Jun 2014.

[3] J Ulmanis, S Häfner, R Pires, E D Kuhnle, M Weidemüller, and E Tiemann. Universality of weakly bound dimers and efimov trimers close to Li–Cs Feshbach resonances. *New Journal of Physics*, 17(5):055009, 2015.

[4] J. Ulmanis, S. Häfner, R. Pires, F. Werner, D. S. Petrov, E. D. Kuhnle, and M. Weidemüller. Universal three-body recombination and Efimov resonances in an ultracold Li-Cs mixture. *Phys. Rev. A*, 93:022707, Feb 2016.

[5] A. A. Blinova, M. G. Boshier, and Eddy Timmermans. Single impurities in a Bose-Einstein condensate can make two polaron avors. *arXiv*, 2013.

[6] Pietro Massignan, Matteo Zaccanti, and Georg M Bruun. Polarons, dressed molecules and itinerant ferromagnetism in ultracold fermi gases. *IOP Publishing Rep. Prog. Phys.*, 77(034401), 2014.

[7] Jozef T Devreese and Alexandre S Alexandrov. Fröhlich polaron and bipolaron: recent developments. *Reports on Progress in Physics*, 72(6):066501, 2009.

[8] Marc Repp. *Interspecies Feshbach Resonances in an Ultracold, Optically Trapped Bose-Fermi Mixture of Cesium and Lithium.* PhD thesis, Ruperto-Carola-University of Heidelberg, 2013.

[9] Carmen Renner. Design and characterization of a dual-wavelength high-resolution imaging system. Master's thesis, University of Heidelberg, 2014.

[10] Andor. *Andor iKon M manual.*

[11] Chris McFee. An introduction to ccd operation. `http://www.mssl.ucl.ac.uk/www_detector/ccdgroup/optheory/ccdoperation.html`. Accessed: 23 March 2016.

[12] Allied Vision. Guppy f-038 datasheet.

[13] M. Repp, R. Pires, J. Ulmanis, R. Heck, E. D. Kuhnle, M. Weidemüller, and E. Tiemann. Observation of interspecies ^{6}Li-^{133}Cs Feshbach resonances. *Phys. Rev. A*, 87:010701, Jan 2013.

[14] *Skript zum Versuch F36 – Teil I "Wellenfrontanalyse mit einem Shack-Hartmann-Sensor" des Fortgeschrittenen-Praktikums II der Universitaet Heidelberg fuer Physiker.*

[15] Timo Bastian Ottenstein. A new objective for high resolution imaging of Bose-Einstein condensates. Master's thesis, University of Heidelberg, 2006.

[16] Simon Murmann. Toward the exact detection of mesoscopic atom numbers. Master's thesis, University of Heidelberg, 2011.

[17] Daniel A. Steck. Quantum and atom optics. Available online at `http://steck.us/teaching`, April 2014. revision 0.9.10.

[18] W. Ketterle, D. S. Durfee, and D. M. Stamper-Kurn. Making, probing and understanding Bose-Einstein condensates. In M. Inguscio, S. Stringari, and C.E. Wieman, editors, *Proceedings of the International School of Physics "Enrico Fermi"*, Course CXL, pages 67–176. IOS Press, Amsterdam, 1999.

[19] Stephan Helmrich. Improving optical resolution by noise correlation analysis. Master's thesis, 2013.

[20] Wolfgang Ketterle and Martin W. Zwierlein. Making, probing and understanding ultracold fermi gases. In W. Ketterle M. Inguscio and C. Salomon, editors, *Proceedings of the International School of Physics Enrico Fermi*, volume Course CLXIV, page 95. IOS Press, Amsterdam, 2008.

[21] Robert Heck. All-optical formation of an ultracold gas of fermionic lithium close to quantum degeneracy. Master's thesis, Ruperto-Carola-University of Heidelberg, 2012.

[22] Y. Shin, M. W. Zwierlein, C. H. Schunck, A. Schirotzek, and W. Ketterle. Observation of phase separation in a strongly interacting imbalanced fermi gas. *Phys. Rev. Lett.*, 97:030401, Jul 2006.

[23] Martin W. Zwierlein, Christian H. Schunck, André Schirotzek, and Wolfgang Ketterle. Direct observation of the superfluid phase transition in ultracold fermi gases. *Nature*, 442(7098):54–58, July 2006.

Danksagung

Ich möchte an dieser Stelle die Gelegenheit nutzen, mich bei Prof. Dr. Matthias Weidemüller zu bedanken, der es mir ermöglicht hat in dieser Arbeitsgruppe meine Bachelorarbeit abzuschließen. Meinen herzlichsten Dank widme ich des weiteren Dr. Juris Ulmanis. Mit seiner Begeisterung für die Physik konnte er mich für die Welt der ultrakalten Quantengase gewinnen und mit seiner vielen Zeit konnte er aus jedem Problem interessante Physik gestalten. Des weiteren bedanke ich mich außerdem bei Stephan Häfner, der mit seinem physikalischen Geschick Fehler schnell entdecken konnte und mir somit Zeit und Frustration erspart hat. Mit Manuel Gerken konnte ich jeder physikalischen Fragestellung, ob einfach oder komplex, auf den Grund gehen und durch ihn wurden meine Stunden im Büro erst unterhaltsam. Ich habe die Zeit in dieser Arbeitsgruppe sehr genossen, dafür gebührt mein herzlichsten Dank.

Statement of Authorship

I herewith declare that this thesis was solely composed by myself and that it constitutes my own work unless otherwise acknowledged in the text. I confirm that any quotes, arguments or concepts developed by another author and all sources of information are referenced throughout the thesis. This work has not been accepted in any previous application for a degree.

Heidelberg, April 1, 2016

_____

Signature